

# High-Resolution Intracellular Recordings Using a Real-Time Computational Model of the Electrode

Romain Brette,<sup>1,2,3,\*</sup> Zuzanna Piwkowska,<sup>1,3</sup> Cyril Monier,<sup>1</sup> Michelle Rudolph-Lilith,<sup>1</sup> Julien Fournier,<sup>1</sup> Manuel Levy,<sup>1</sup> Yves Frégnac,<sup>1</sup> Thierry Bal,<sup>1</sup> and Alain Destexhe<sup>1</sup>

<sup>1</sup>Unité de Neurosciences Intégratives et Computationnelles (UNIC), CNRS, 91198 Gif-sur-Yvette, France

<sup>2</sup>Équipe Odyssée (ENS/INRIA/ENPC), Département d'Informatique, École Normale Supérieure, F-75230 Paris Cedex 05, France

<sup>3</sup>These authors contributed equally to this work

\*Correspondence: [brette@di.ens.fr](mailto:brette@di.ens.fr)

DOI 10.1016/j.neuron.2008.06.021

## SUMMARY

Intracellular recordings of neuronal membrane potential are a central tool in neurophysiology. In many situations, especially *in vivo*, the traditional limitation of such recordings is the high electrode resistance and capacitance, which may cause significant measurement errors during current injection. We introduce a computer-aided technique, Active Electrode Compensation (AEC), based on a digital model of the electrode interfaced in real time with the electrophysiological setup. The characteristics of this model are first estimated using white noise current injection. The electrode and membrane contribution are digitally separated, and the recording is then made by online subtraction of the electrode contribution. Tests performed *in vitro* and *in vivo* demonstrate that AEC enables high-frequency recordings in demanding conditions, such as injection of conductance noise in dynamic-clamp mode, not feasible with a single high-resistance electrode until now. AEC should be particularly useful to characterize fast neuronal phenomena intracellularly *in vivo*.

## INTRODUCTION

Intracellular recordings of neuronal membrane potential ( $V_m$ ) are currently the only tool for studying the integration of excitatory synaptic inputs, inhibitory inputs, and intrinsic membrane currents underlying the spiking response. *In vivo*, these recordings are done using either single high resistance sharp microelectrodes with low capacitance (Steriade et al., 2001; Wilent and Contreras, 2005a; Crochet et al., 2006; Higley and Contreras, 2007; Haider et al., 2007; Paz et al., 2007) that are also used in some adult *in vitro* preparations (Thomson and Deuchars, 1997; Shu et al., 2003) or using single patch electrodes that can display a whole range of resistances and capacitances depending on the age and species of the animal (rather low values could be obtained in rats up to a certain age [see Margrie et al., 2002], as well as in cat [Borg-Graham et al., 1998; Monier et al., 2008]; resistances closer to those of sharp electrodes were used in other studies, [see Pei et al., 1991; Hirsch et al., 1998;

Anderson et al., 2000; Wehr and Zador, 2003; Mokeichev et al., 2007]). The problem inherent to such single-electrode recordings is that the injected current biases the measurement because of the voltage drop through the electrode. This electrode bias imposes restrictions on the use of advanced electrophysiological techniques, such as voltage clamp or dynamic clamp (Robinson and Kawai, 1993; Sharp et al., 1993; Prinz et al., 2004), which require injection of a current dependent on the simultaneously recorded  $V_m$ . These techniques are essential for dissecting the role of specific intrinsic and synaptic channels in neuronal function. In the present paper, we introduce Active Electrode Compensation (AEC), a method to compensate for the electrode bias with unprecedented accuracy, based on a model of the electrode interfaced in real time with the electrophysiological setup. AEC opens the way for the improved and simplified use of these advanced techniques in many preparations requiring high resistance and/or capacitance electrodes: for example, *in vivo* recordings of cortical neurons.

Electrode compensation circuits implemented in intracellular amplifiers usually reflect the assumption that the electrode is equivalent to a simple RC (resistor and capacitor) circuit (Thomas, 1977), but this simplification does not account for distributed capacitance and the resulting compensation produces artifactual voltage transients (Figure 1A, bridge compensation, middle). In situations where the injected current depends on the  $V_m$ , the artifacts are injected back and can be amplified by the control loop, which leads to oscillatory instabilities (Figure 1A, bridge compensation during dynamic clamp, right). An option for voltage clamp, and the only one for dynamic clamp when electrode resistance is high, is to use a discontinuous mode, alternatively injecting current and recording the  $V_m$  (Brennecke and Lindemann, 1971, 1974a, 1974b; Finkel and Redman, 1984) with a frequency set by the electrode time constant (typically 1.5–3 kHz with sharp electrodes in our experiments in cortical neurons *in vitro* and *in vivo*). Unfortunately, the alternation method is valid only when the electrode response is at least two orders of magnitude faster than the recorded phenomena (Finkel and Redman, 1984), because the membrane response must be quasilinear in the sampling interval. Moreover, recordings in discontinuous modes are very noisy and sampling frequency is limited, which makes the precise recording of fast phenomena like spikes impossible (Figure 1B).

The AEC method we propose here allows the sampling of the  $V_m$  during current injection with a frequency only limited by the

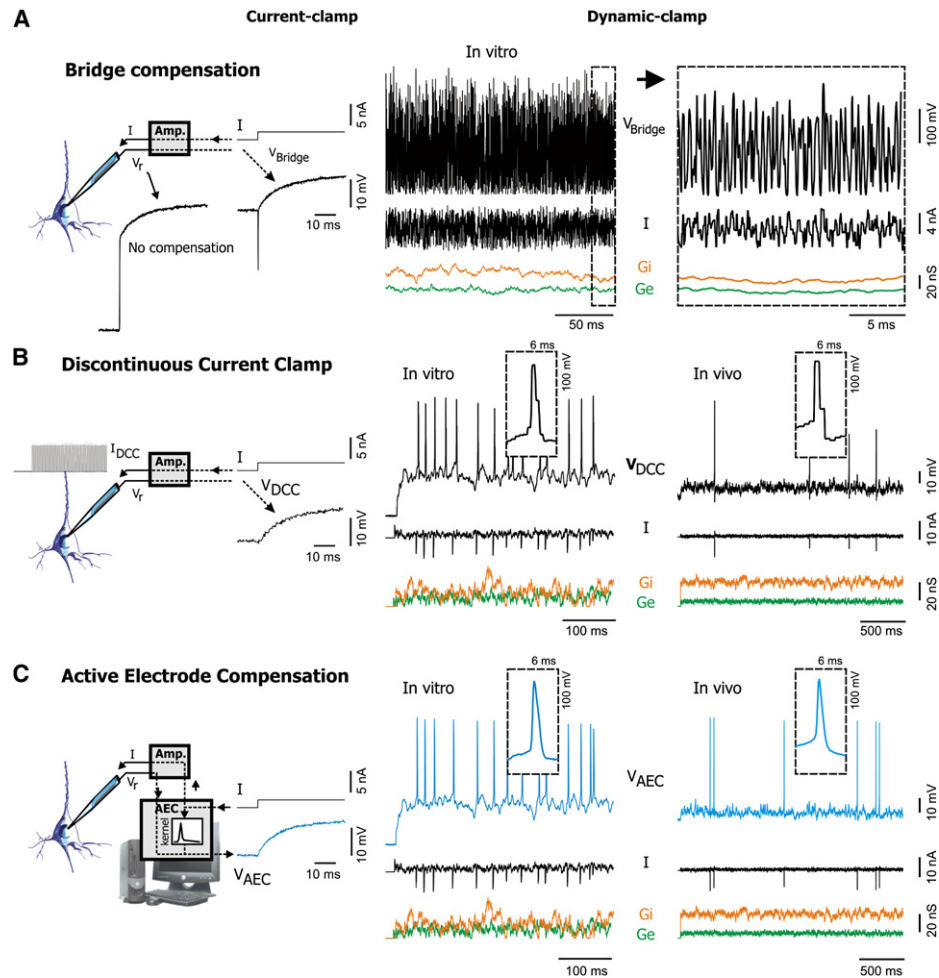


**Figure 1. Compensating for the Electrode Response during Simultaneous Current Injection and Recording of Neuronal Membrane Potential**

(A) “Bridge” compensation performed by the amplifier (left). The capacitive properties of the electrode lead to a capacitive transient at the onset of the response to a current step (middle). A loop is established between  $V_m$  recording and current injection when inserting virtual conductances G in dynamic clamp (right). When fast fluctuating conductances are inserted, the transients lead to a strong “ringing” oscillation in the recorded potential  $V_{Bridge}$  and the injected current I ( $R_e = 93 \text{ M}\Omega$ , IB cell).

(B) Discontinuous current clamp (DCC; see text for details) in vitro and in vivo. There is no capacitive transient at the onset of the response to a current step (middle). Conductance injection using dynamic clamp can be performed (right) without oscillations, but the sampling resolution of the  $V_m$  is low, as seen when zooming in on single spikes (see insets).

(C) Active electrode compensation (AEC) in vitro and in vivo, a new method for high-resolution  $V_m$  recording during simultaneous current injection. This digital compensation is performed in real time by a computer (left). No capacitive transient is seen at the onset of the response to a current step (middle;  $R_e = 87 \text{ M}\Omega$ , RS cell, for all the current step examples shown). Conductance injection using dynamic clamp (right;  $R_e = 63 \text{ M}\Omega$ , RS cell in vitro;  $R_e = 103 \text{ M}\Omega$ , RS cell in vivo) is performed with a high  $V_m$  sampling frequency (10 kHz) so that the shape of single spikes can be resolved (see inset).

speed of the computer used for the digital convolution at the core of the technique (Figure 1C). In the following, we describe and validate the method in demanding experimental situations: high resistance sharp microelectrode recordings for both current-clamp with fast current injection and dynamic-clamp protocols. We performed such recordings in vitro and in vivo in two experimental preparations widely used for the study of mammalian cortical function: in slices of visual cortex from adult animals (in our case, guinea pigs and ferrets) and in the primary visual cortex of the anaesthetized and paralyzed cat. These examples illustrate that with AEC, it is possible, in cases when single high

resistance electrodes are used, to inject white noise in a cell at a high sampling frequency and to accurately inject complex conductance stimuli with the goal of precisely analyzing high frequency features of the cell’s response, such as the onset of spikes. More generally, AEC will be especially useful for the study of any electrical neuronal phenomenon happening on the timescale of the electrode time constant, and it widens in an important way the repertoire of electrophysiological protocols easily applicable to the study of central mammalian neurons in vivo and of other preparations where very low resistance electrodes cannot be routinely employed.

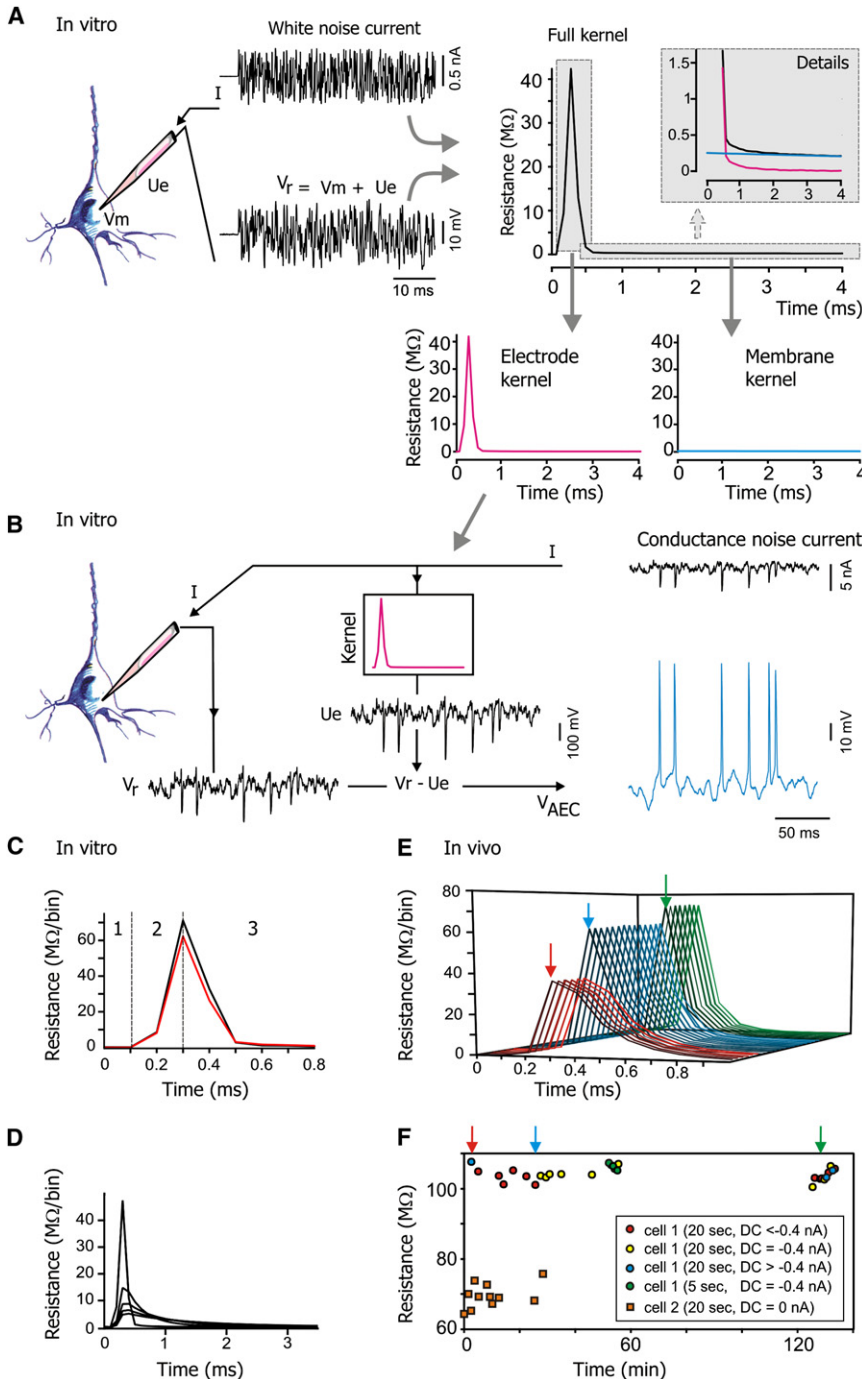


**Figure 2. The Two Stages of the AEC Method**

(A) Electrode properties are estimated first: white noise current is injected into the neuron, and the total response  $V_r$ , corresponding to the sum of the membrane potential  $V_m$  and the voltage drop across the electrode  $U_e$ , is recorded ( $R_e = 76 \text{ M}\Omega$ , RS cell recorded in vitro). The crosscorrelation between the input current and the output voltage gives the kernel (or impulse response) of the neuronal membrane and electrode system (full kernel, right). The neuronal membrane kernel has a total resistance of  $31 \text{ M}\Omega$  here; however, the response is spread over a long time. The vertical axis gives the resistance of each  $0.1 \text{ ms}$  time bin, so that the resistance value is very small for each such bin (though not 0, see detail of black and blue traces in the inset) but adds up to  $31 \text{ M}\Omega$  when all the bins are added (not all the bins are shown on the figure). This full kernel is separated into the electrode kernel and the membrane kernel.

(B) The electrode kernel is then used in real time for electrode compensation: the injected current is convolved with the electrode kernel to provide the electrode response,  $U_e$ , to this current.  $U_e$  is then subtracted from the total recorded voltage,  $V_r$ , to yield the  $V_m$  ( $V_{AEC}$ ).

(C) Kernel of the same electrode estimated in the slice before the impalement of a neuron (black,  $R_e = 118 \text{ M}\Omega$ ) and, after impalement, in a cell (red,  $R_e = 108 \text{ M}\Omega$ , IB cell). The numbers above the graph indicate the three phases of a typical electrode kernel, described in detail in the main text.

(D) Electrode kernels obtained in the slice for different levels of capacitance neutralization (the sharpest kernel corresponds to the highest level of capacitance neutralization;  $R_e = 87\text{--}89 \text{ M}\Omega$ ).

(E) Electrode kernels obtained in vivo at different times after the impalement of a cell ( $R_e = 103 \text{ M}\Omega$ , RS cell). The setting of the capacitance neutralization circuit was changed by the experimentalist when indicated by arrows.

(F) Temporal stability of the electrode resistance in vivo (cells 1 and 2 are RS cells). Cell 1 is the same cell as shown in (E), and arrows indicate changes in the setting of the capacitance neutralization circuit. Kernels were estimated using 5 or 20 s white noise current injections. In addition, different constant current levels (DC) were injected, preventing spiking activity during the estimation. In all cases but for the blue points, moderate spiking did not perturb the kernel estimation.

**RESULTS**

**A Method Based on a General Model of the Electrode**

The essential idea behind the AEC method is to represent the electrode by an arbitrarily complex linear circuit, extract the properties of this circuit for each particular recording (Figure 2A), and actively compensate for the effect of the electrode by subtracting the voltage drop through this circuit from the recording (Figure 2B). The classic compensation methods,

“bridge” compensation and capacitance neutralization, are equivalent to modeling the electrode as a resistor plus a capacitor (RC circuit), but this model proves too simple in many practical situations. We used a more general model of the electrode as an unknown linear circuit. A particular case of such a linear circuit could be two resistors and two capacitors, as hypothesized by Roelfsema et al. (2001). It could also be much more complicated: in fact, our results show that elements of the amplifier (e.g., filters) should be included in the recording circuit.

The voltage across the electrode  $U_e$  is modeled as the convolution of the injected current  $I_e$  and a kernel  $K_e$  that characterizes the electrode:

$$U_e(t) = (K_e * I_e)(t) = \int_0^{+\infty} K_e(s) I_e(t-s) ds.$$

Thus, the voltage across the electrode depends linearly on all past values of the injected current: it is the sum of all these past values weighted by the coefficients of the kernel  $K_e$ . This formulation encompasses any time-invariant linear model, e.g., a circuit with a resistor and a capacitor (the kernel  $K_e$  is then an exponential function). For any linear model, the kernel completely characterizes the system, i.e., it allows the calculation of the system's response to any input. For digitally sampled signals, the formula reads:

$$U_e(n) = \sum_0^{+\infty} K_e(p) I_e(n-p) \quad (1)$$

(But, the discrete and continuous kernels are not generally identical. See the [Supplemental Data](#) available online.)

The procedure consists in two passes: (1) measure the electrode kernel, i.e., the values of  $K_e(p)$  (Figure 2A, right), (2) inject and record at the same time in continuous mode, with the true  $V_m$  recording obtained by subtracting the voltage across the electrode  $U_e$  from the raw recording. The compensation involves the digital convolution of  $I$  with  $K_e$  to obtain  $U_e$ , which is performed in real time by a computer (Figure 2B).

### Measuring Electrode Properties in the Cell

For small injected currents, the response of the cell can also be considered linear, so that the recorded potential can be expressed as the linear convolution  $V_r = V_{rest} + K * I$ , where  $V_{rest}$  is the resting potential and  $K$  is the total kernel comprising both the electrode kernel  $K_e$  and the membrane kernel  $K_m$  and fully characterizing the system consisting of the electrode and the cell. We derive  $K$  from the recorded response to a known injected current and then we separate the contributions of the electrode and the membrane (Figure 2A; see the [Experimental Procedures](#)). Electrode properties before and after cell impalement can be quite different (Figure 2C), so it is essential to estimate the electrode kernel in the neuron by means of this separation.

We inject 5–20 s of noisy current consisting of a sequence of independent random current steps (white noise) at sampling resolution (0.1 ms) with amplitude uniformly distributed between  $-0.5$  nA and  $0.5$  nA in most cases. In principle, any current could be used provided it is small enough to prevent spiking and nonlinear effects from the cell (see the [Supplemental Data](#) for details about how to set the current intensity), but our choice was not arbitrary: a uniform amplitude distribution makes the best use of the D/A converters in the acquisition board (provided their range is adjusted accordingly), while using a fast-varying current with minimum autocorrelation enhances the electrode contribution in the recording relative to the membrane contribution, because the electrode response is at least one order of magnitude faster than the membrane response. In vivo, we injected, in addition, a constant negative

current (Figure 2F) to prevent spiking. The kernel  $K$  is then derived mathematically from the autocorrelation of the current and the correlation between the current and the recorded potential (see [Experimental Procedures](#)).

To split the total kernel  $K$  into the electrode kernel  $K_e$  and the membrane kernel  $K_m$ , we use two facts: first, the electrode kernel is very short compared to the membrane kernel, so that after a couple of milliseconds ( $p > 50$ , i.e., 5 ms at 10 kHz),  $K_e(p)$  vanishes and  $K(p) \approx K_m(p)$ . Second, if the injected current is small enough, the membrane response is mostly linear and can be approximated on short time scales by a decaying exponential  $K_m(t) = \frac{R}{\tau} e^{-t/\tau}$  ( $t = p \Delta t$ , where  $\Delta t$  is the sampling step;  $R$  and  $\tau$  are passive membrane parameters). Thus, we estimate the membrane kernel  $K_m$  from the tail of the total kernel  $K$  (least square fitting to an exponential) and deduce the electrode kernel  $K_e$  (see the [Experimental Procedures](#); Figure 2A; see also Figure S1). We tested the sensitivity of the method to these two hypotheses in numerical simulations: (1) the estimated electrode kernel degrades continuously as the ratio of electrode and membrane time constants ( $\tau_e/\tau_m$ ) increases (Figure S1D) and remains acceptable for ratios better than 1/10 (the error in electrode resistance is about 10%, and AEC can still be used for compensating the voltage in dynamic-clamp protocols, see Figure S3, right column); (2) the membrane kernel deviates from a single exponential function in the presence of a dendritic tree, and fast passive dendritic contributions can be confused with the electrode response, but the impact on the estimated electrode kernel remains small (Figure S4). In practice, nonlinear membrane properties (even action potentials if the firing rate is not too large) have a small impact on the estimation of the electrode kernel (see Figure 2F, blue points, and Figure S4H), the important requirement being the linearity of the electrode (see below).

In fact, the electrode kernel  $K_e$  captures not only the characteristics of the electrode, but also of the recording device, i.e., the whole circuit between the digital output of the computer and the tip of the electrode, including all circuits in the amplifier (e.g., capacitance neutralization) and acquisition filters, but not subsequent digital signal processing. All measured electrode kernels consisted of 3 phases (Figure 2C): (1) a short phase where the kernel vanishes, (2) a sharp but noninstantaneous increase for about 0.2 ms, and (3) a decrease. The first phase corresponds to the feedback delay of the acquisition system and always lasts 2 sampling steps (0.2 ms). The second, noninstantaneous phase also appears when the amplifier is plugged into an electronic circuit, named the model cell, consisting of a resistor modeling the electrode and a resistor plus a capacitor modeling the neuron membrane (data not shown): its nonzero rise time is likely due to the electronics of the acquisition system rather than to the electrode properties per se. The third phase varies between experiments and, when fitted by an exponential, displays a time constant around 0.1 ms ( $0.11 \pm 0.09$  ms,  $n = 67$  cells in vitro, for maximal levels of capacitance neutralization by the amplifier). Lowering the level of capacitance neutralization increases this time constant (Figure 2D). In vivo, the time constant estimated in 4 cells was of the same order of magnitude (for example, 0.1 ms for the cell [Figure 2E] with maximal capacitance neutralization).

### Estimating the Electrode Resistance

As a first test of the method, we assessed the quality of the estimation of the electrode resistance derived from our measurement of the electrode kernel. The electrode resistance,  $R_e$ , is defined as the ratio of the stationary voltage across the electrode over the amplitude of a constant injected current. It equals the integral of the electrode kernel (or the sum in the digital formulation). In 67 cortical neurons in vitro, we compared the  $R_e$  estimated from the kernel with the  $R_e$  estimated by manually adjusting the “bridge” compensation on the amplifier and found a difference of only  $1.4 \pm 4.2\%$  (AEC – bridge;  $n = 67$  cells). Bridge compensation only provides an estimate of the electrode resistance, but AEC also deals with the effects of the residual capacitance of the electrode (after maximal neutralization, residual electrode capacitance was  $1.3 \pm 1.3$  pF as assessed from the decay phase of the electrode kernel;  $n = 67$  cells).

The linearity of the electrode is an important assumption of the AEC method, since we consider that the electrode response can be fully characterized by the kernel  $K_e$ . It has been described that for sharp electrodes,  $R_e$  can change with the amplitude of injected current, presumably due to differences in ion concentrations inside and around the pipette tip (Purves, 1981). This might be a problem since during AEC, the same kernel, with a fixed  $R_e$ , is used for predicting the electrode response to all levels of injected current. We systematically tested for this effect in 23 intracellular recordings in vitro (using 20 different electrodes) by estimating the electrode kernel in the recorded cell while simultaneously injecting different levels of constant current in addition to the white noise current (Figure S2). The degree of nonlinearity  $\lambda$  can be expressed in  $M\Omega/nA$  as a current-dependent change in resistance, and the resulting voltage measurement error for a given depolarization  $\Delta V$  (induced by constant current injection) is then  $(\lambda/R_m^2) \times \Delta V^2$ , where  $R_m$  is the membrane resistance. Across all tested electrodes, this slope averaged  $-2.2 (\pm 5.0)$   $M\Omega/nA$ , giving, for a cell with an  $R_m$  of 60  $M\Omega$ , a voltage error  $-0.0006$  mV/mV<sup>2</sup> (e.g.,  $-0.55$  mV for 30 mV depolarization). In 9 out of 23 cases, we found that the correlation between  $R_e$  and the level of constant injected current was not significant (see Figure S2), meaning that the current-dependent variability of the electrode resistance was comparable to the intrinsic variability of the electrode resistance (for these electrodes, the measured nonlinearity was  $-0.5 \pm 1.1$   $M\Omega/nA$ ). Thus, the kernel estimation procedure provides a fast and automated way to measure electrode nonlinearities in the cell and possibly discard some recordings if the change of  $R_e$  during given current injections leads to unacceptable errors in the recorded  $V_m$ .

Electrode nonlinearities are generally described as slow processes (Purves, 1981), which was our working hypothesis, but we also checked in the dynamic-clamp protocols that large, transiently injected currents did not impair the electrode compensation, as could result from fast nonlinearities (see below). In addition, in 4 intracellular recordings (using 3 electrodes), we compared electrode kernels obtained by injecting 0.5 or 1 nA of white noise current and found, on average, a difference of only  $-0.1$   $M\Omega$  (range  $-0.9$  to  $0.5$ ; Figure S2B), which indicates that possible electrode nonlinearities (i.e., changes in  $R_e$ ) do not manifest themselves for very fast current injections.

In vivo, we found that electrode properties could remain stable for up to 2 hours, as assessed with kernel estimations obtained repetitively and also when using different constant current injections and different durations of white noise injection (Figures 2E and 2F).

### White Noise Current Injection

A first application of the AEC method is the possibility to accurately record the response of a neuron to an injection of white noise current sampled at a high frequency (10 kHz with our system). This type of stimulus has been used to characterize neuronal response properties (Bryant and Segundo, 1976). We confirmed ( $n = 18$  injections in 3 cortical cells in vitro and  $n = 8$  in 2 cortical cells in vivo) that the subthreshold response of neurons to such an injection corresponds to the theoretical prediction based on the passive parameters of the cell (Figure 3A). The recorded  $V_m$  distributions closely matched the predicted distributions (Figures 3B and 3D) ( $8.9 \pm 9.9\%$  relative error on the standard deviation of the distributions for in vitro recordings), and power spectra of the response matched the theoretical power spectra up to a frequency of 500 Hz (Figure 3C). In addition, spikes occurring during the white noise injection could be recorded with good temporal resolution (Figure 6C; a higher sampling frequency might be required for fast spiking cells). Attempts to inject a white noise current sampled at 10 kHz with DCC at 1 to 2 kHz switching frequency failed to match the prediction (Figures 3B–3D), which was expected since the input current was changing significantly faster than the sampling clock of the DCC. The response to white noise injection can also be characterized using the crosscorrelation between injected current and recorded  $V_m$ , which shows unwanted electrode contributions and distortions in both Bridge mode and DCC when compared to AEC (Figure S6). Generally, white noise inputs are an interesting choice for probing the input-output functions of systems due to their lack of autocorrelation, and they could now, with AEC, be more widely applied in single-cell neurophysiology.

### Dynamic Clamp

Our initial motivation for developing the AEC method was to improve the quality of dynamic clamp performed with single high resistance electrodes. Dynamic clamp (Robinson and Kawai, 1993; Sharp et al., 1993) is an electrophysiological technique for mimicking ion channels activating and inactivating in a cellular membrane. It can be advantageously employed in a variety of contexts, from the addition and subtraction of various intrinsic channels to neurons and the scanning of their kinetic parameters, through the manipulation of synaptic channels activated by various configurations of presynaptic inputs, up to the construction of hybrid networks in which biological cells interact with model cells simulated in real time (see Prinz et al. [2004] for a review). The technique relies on a loop in which the current injected into the cell is a function of the recorded  $V_m$ . The current flowing through ion channels at time  $t$  depends on both the channels' total conductance  $g(t)$  and the driving force  $V_m(t) - E_{rev}$  (where  $E_{rev}$  is the reversal potential for the considered ions):  $I(t) = g(t) \times (V_m(t) - E_{rev})$ . In dynamic-clamp experiments, intrinsic or synaptic ion channels are modeled by given  $g(t)$  and  $E_{rev}$ .

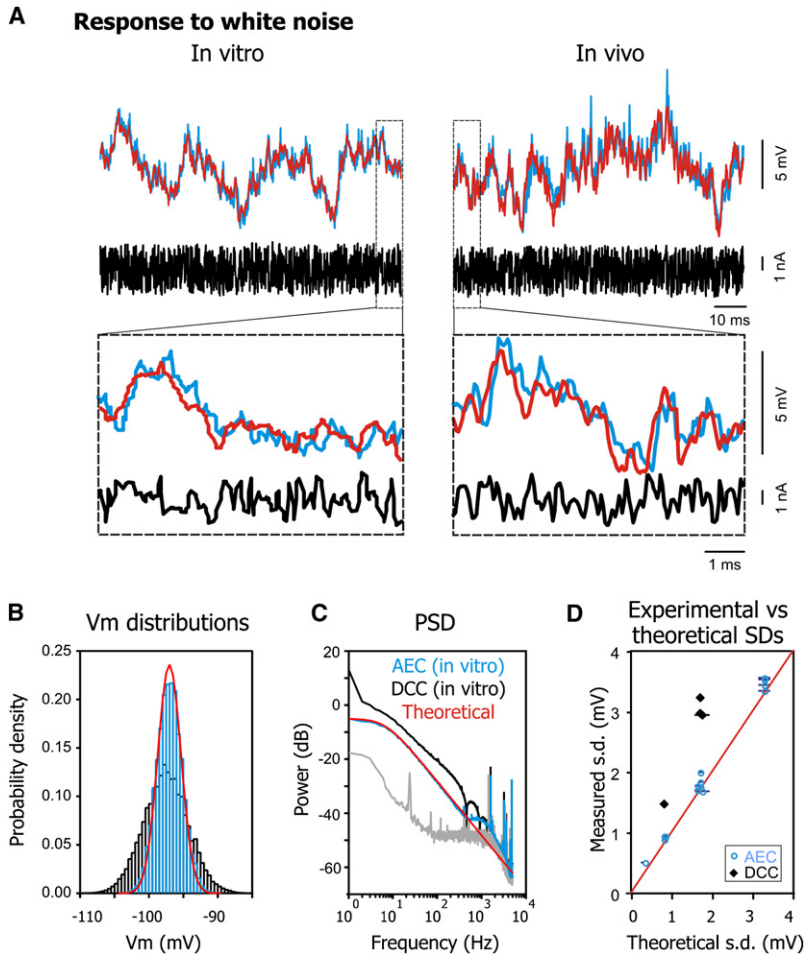


**Figure 3. White Noise Current Injection Using AEC**

(A) Example  $V_m$  responses of one neuron recorded in vitro (left;  $R_e = 63 \text{ M}\Omega$ , RS cell) and another one in vivo (right;  $R_e = 103 \text{ M}\Omega$ , RS cell) using AEC (blue), and  $V_m$  responses obtained by simulating the same noise injection in a point model neuron using the leak parameters of the recorded cell (red). The injected current is displayed below (black). (B)  $V_m$  distribution recorded using AEC (blue), DCC (black), and theoretical distribution in response to the same injected current (red).

(C) Power spectral density (PSD) of the  $V_m$  recorded using AEC (blue), DCC (black), and theoretical PSD in response to the same injected current (red). The PSD of the baseline  $V_m$  (gray) shows that the bump in the higher frequencies is not due to AEC, but rather to the power of recording noise reaching the level of the signal. Data for (B) and (C) was obtained in an RS cell in vitro different from the one in (A), with  $R_e = 94 \text{ M}\Omega$ .

(D) Pooled data: standard deviation of the  $V_m$  distributions obtained using AEC (blue, open) or DCC (black, filled) versus theoretical standard deviation based on leak parameters of the recorded neuron (error bars represent the range of theoretical standard deviations obtained for different estimates of passive cell parameters; solid line,  $y = x$ ).

implemented in a computer, and  $I(t)$  is calculated in real time using the  $V_m(t)$  of the recorded cell. It is crucial, in this equation, to use the real  $V_m$  of the cell, uncontaminated by electrode artifacts which can lead to oscillatory instabilities or, simply, inaccurate results. With bridge compensation, dynamic clamp injections are unstable if the conductance is too large; theoretical analysis (see Supplemental Data) shows that this critical conductance is determined by the electrode resistance:  $g_c = 1/R_e$  (same magnitude as the membrane leak conductance in our experiments). With complete digital compensation of the electrode, the critical conductance is theoretically limited by the sampling frequency  $f$ :  $g_c = \tau_m f / (4R_m)$ , where  $\tau_m$  is the membrane time constant and  $R_m$  is the membrane resistance (for typical values in our experiments,  $g_c$  is 25 times the leak conductance).

We tested the performance of the AEC method in cortical neurons in vitro and in vivo with three different dynamic-clamp protocols of increasing complexity: square conductance pulses and fluctuating synaptic conductance input without and with additional discrete AMPA synaptic inputs. We compared AEC to the only alternative method, DCC, and, whenever possible, to theoretical predictions of the response. Dynamic-clamp injections of fluctuating synaptic conductance input provide the way to extend, to real cortical neurons, the study of the integrative properties of cells submitted to a massive synaptic bom-

bardment from the cortical network, a topic extensively investigated using computational models (see Destexhe et al. [2003] for a review).

**Square Conductance Pulses**

We first injected a simple conductance stimulus for which the cell's response can be computed analytically, assuming we are in the passive regime and the leak parameters of the cell are known (from the response to small current pulses). This choice enabled us to compare the responses obtained in AEC and in DCC with theoretical predictions, but this time with dynamic clamp rather than current clamp. The stimulus was a square wave of alternating "excitatory" ( $E_{excitation} = V_{rest} + 10$ ) and "inhibitory" ( $E_{inhibition} = V_{rest} - 10$ ) conductance pulses (Figure 4A). Different conductance amplitudes (range 10–100 nS) and frequencies (range 10–1000 Hz) were scanned ( $n = 57$  AEC-DCC pairs in total in 8 cells in vitro).

To avoid alignment problems and to separate the quality of the response shapes from the amount of recording noise, we represented the responses in a phase space where they appear as noisy squares and can be compared to theoretical predictions (see Experimental Procedures, Supplemental Data, and Figure 4B). Three error measures were derived from the comparison of the actual response to the theoretical prediction: the "side" measure quantifies the amplitude of the  $V_m$  response, the "tilt" measure quantifies the shape of the response (between a triangular wave and a square wave), and the "distance" measure quantifies the amplitude of the noise around the best-fit response. All those error measures are significantly lower for AEC (tilt error,  $5.7 \pm 9.2^\circ$ ; side error,  $21.2 \pm 34\%$ ; distance,  $0.2 \pm 0.16 \text{ mV}$ ) than for DCC (tilt error,  $14.6 \pm 11.8^\circ$ ; side error,  $66.6 \pm 86\%$ ; distance,  $0.43 \pm 0.49 \text{ mV}$ ) ( $p < 0.0001$  for all three error measures,  $n = 56$ ). Figure 4C (top and middle) shows measured versus theoretical values for tilt and side. In

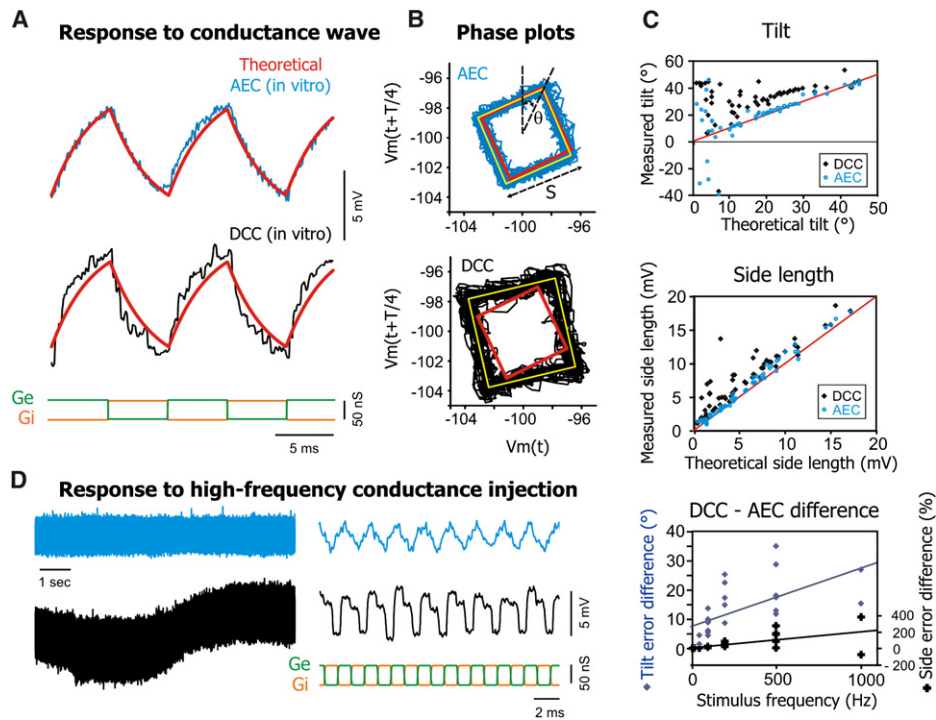


**Figure 4. Conductance Square Wave Injection in Dynamic Clamp**

(A) Example  $V_m$  responses ( $R_e = 71 \text{ M}\Omega$ , RS cell) to a square wave (50 nS amplitude) of alternating excitatory (green) and inhibitory (orange) conductances using AEC (top, blue) or DCC (black, middle). The response obtained by simulating the same conductance injection in a point model neuron using the passive parameters of the recorded cell is shown in red.

(B) Phase plots of the  $V_m$  responses shown in (A). Instead of plotting  $V_m$  versus time, here  $V_m$  at time  $t + T/4$  is plotted against  $V_m$  at time  $t$  ( $T$ : period of the injected wave). Red: theoretical phase plot calculated using the stimulus parameters and the cell's leak parameters. Yellow: square providing the best fit to the experimental phase plot. Each square is characterized by its side length,  $S$ , and its tilt relative to the vertical,  $\theta$  (see the [Experimental Procedures](#)).

(C) Pooled data from all cells and injection parameters used (AEC, blue open circles; DCC, black filled diamonds). Tilt of the recorded phase plot versus the theoretical tilt (top), side length of the recorded phase plot versus theoretical side (middle), and difference (DCC – AEC) between tilt and side errors (relative to the theoretical prediction) in AEC and in DCC versus square wave frequency.

(D)  $V_m$  response ( $R_e = 89 \text{ M}\Omega$ , RS cell) to high frequency (500 Hz) conductance wave injection (50 nS amplitude), in AEC (blue, top) and DCC (black, bottom). Low frequency oscillations appear in DCC as a result of asynchronous sampling when the frequency of the conductance wave is close to the frequency of the DCC sampling clock (the phase of sampling points with respect to the input slowly drifts).

addition, for all three measures, the advantage of AEC over DCC grows with the waveform's frequency (Figure 4C, bottom; linear regression analyses,  $p < 0.0001$  for tilt and side error difference,  $p = 0.0066$  for distance difference), indicating that AEC allows partly overcoming the limitations due to the low sampling frequency in DCC. Low frequency aliasing artifacts in DCC at very high stimulus frequencies are the most striking examples of these limitations (Figure 4D). In conclusion, AEC allows better quality dynamic-clamp injection of conductance and recording of the  $V_m$  response than DCC, especially for high frequency stimuli.

Large currents were injected transiently at times of switching between excitation and inhibition: up to  $\pm 2 \text{ nA}$  for the highest conductance values. If there were important changes of  $R_e$  with such strong current injection, they would have resulted in an asymmetry between positive and negative parts of the response, which we did not observe, confirming that electrode nonlinearities are probably slow processes that do not develop when strong but transient current passes through the electrode.

### Colored Conductance Noise

We then injected a fluctuating synaptic conductance input consisting of two stochastic variables,  $g_e(t)$  for excitation and  $g_i(t)$  for inhibition (Figure 5A), mimicking cortical synaptic background activity as seen in vivo (Destexhe et al., 2001) ( $n = 6$  AEC-DCC pairs in 5 cells in vitro and  $n = 2$  in 2 cells in vivo; only in vitro data are presented in plots). Such a stimulus allows the investigation of single neuron properties in reduced, mostly silent preparations in vitro in a finely controlled environment more closely resembling the in vivo environment. In addition, we present here an example of such a stimulus applied in vivo: in this context, it allows the selective manipulation of the network activity impacting on a single cell, which is close to impossible to realize by other means such as pharmacology. Previously derived expressions for the  $V_m$  distribution during fluctuating synaptic conductance injection with known parameters (Rudolph and Destexhe, 2003; Rudolph et al., 2004) and for the  $V_m$  power spectrum (Destexhe and Rudolph, 2004) were used to compare responses recorded in both AEC and DCC with a theoretical prediction (see [Supplemental Data](#)). A very good match was

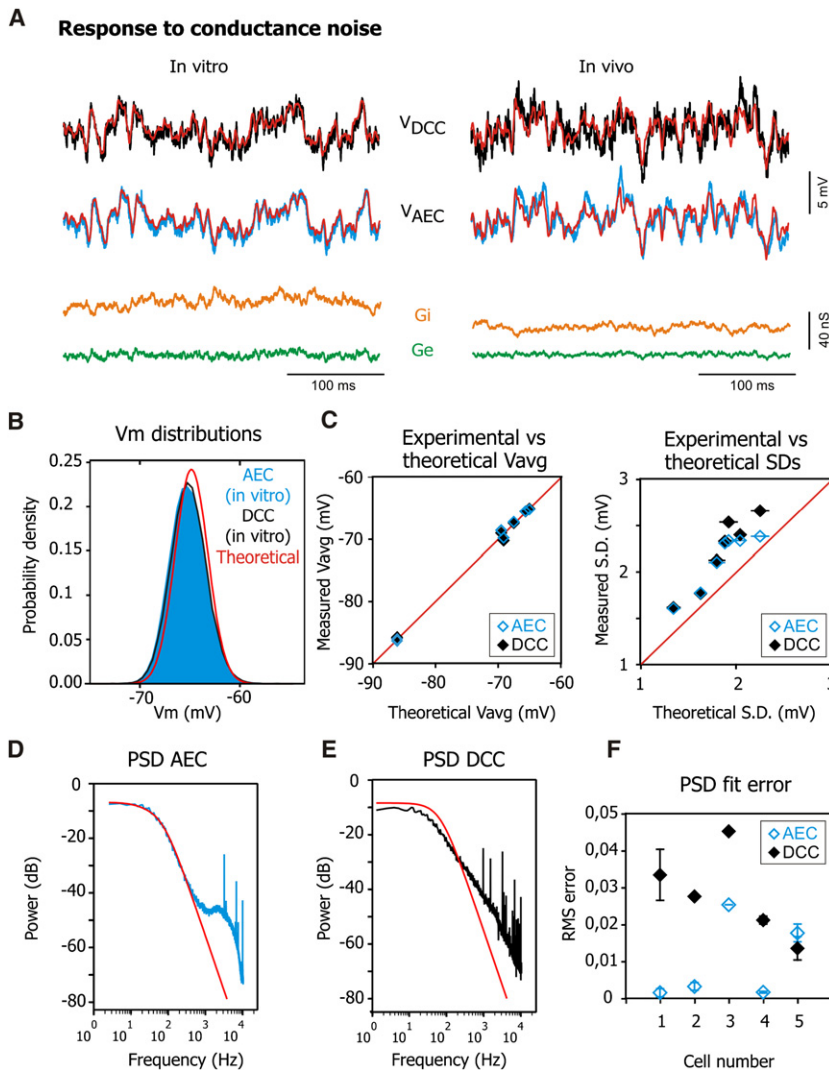


**Figure 5. Colored Conductance Noise Injection in Dynamic Clamp**

(A) Example  $V_m$  responses to fluctuating excitatory (green) and inhibitory (orange) conductances, using AEC (blue) or DCC (black) in vitro (left) and in vivo (right) neurons. The response obtained by simulating the same conductance injection in a point model neuron using the passive parameters of the recorded cell is shown in red.

(B)  $V_m$  distribution using AEC (blue), DCC (black), and theoretical distribution in response to the same injected conductance noise (red).

(C) Pooled data. Mean of the  $V_m$  distributions obtained using AEC (blue, open) or DCC (black, filled) versus theoretical mean based on leak parameters of the recorded neuron (left); standard deviation of the  $V_m$  distributions obtained using AEC (blue, open) or DCC (black, filled) versus theoretical standard deviation based on leak parameters of the recorded neuron (right). (Error bars represent the range of theoretical values obtained when varying estimates of leak parameters by  $\pm 10\%$ ; solid lines,  $y = x$ ).

(D) Power spectral density (PSD) of the  $V_m$  recorded using AEC (blue) and best fit with the theoretical template for the PSD (red).

(E) PSD of the  $V_m$  recorded using DCC (black) and best fit with the theoretical template for the PSD (red). All examples shown (A), (B), (D), and (E) were obtained in the same IB cell in vitro, with  $R_b = 89 \text{ M}\Omega$ , except for the in vivo trace, obtained in an RS cell with  $R_b = 103 \text{ M}\Omega$ .

(F) Pooled data. Root-mean-square (rms) error of the best fit to the experimental  $V_m$  PSDs obtained when using the theoretical template (AEC, blue, open; DCC, black, filled); each point is an average for PSDs obtained from fragments of conductance injections done in the same cell, and error bars are standard deviations).

observed between the predicted average  $V_m$  and the average  $V_m$  measured both in AEC (0.5% average relative error, range 0.003%–1.2%) and in DCC (0.5% average relative error, range 0.1%–1.8%, no significant difference when compared with AEC,  $p = 0.87$ ) (Figures 5B and 5C, left). The measured standard deviations are slightly higher than the prediction (Figures 5B and 5C, right), both in AEC (14.7% average relative error, range 5%–21.6%) and in DCC (18.8% average relative error, range 7.7%–31%), and the error difference between the two methods, albeit small, is significant ( $p = 0.028$ ). The most striking difference between the two methods, however, appeared in the frequency content of the  $V_m$  fluctuations. In 4 out of 5 cells, the power spectral density (PSD) of the  $V_m$  in AEC could be fitted very well with the theoretical template, which provided a good match up to the frequencies where recording noise becomes important (Figure 5D): the PSD scaled as  $f^{-4}$  in the high frequencies as predicted. In DCC, the  $f^{-4}$  scaling was never observed, and the exponent was always smaller (Figure 5E), showing that the correct frequency scaling could only be obtained in AEC (Figure 5F; except for one cell in which all methods yielded erro-

neous scaling). Again, this result demonstrates that AEC is superior to DCC in allowing the accurate investigation of high frequency components of the neuronal response and stresses that this advantage is present not only with simple stimuli like conductance pulses, but also when more realistic stimuli are applied.

#### Detailed Analysis of Spikes

Finally, we compared spikes recorded in both DCC and AEC ( $n = 7$  AEC-DCC pairs in 4 cells in vitro) during an even more complex dynamic-clamp protocol: AMPA excitatory synaptic inputs (Destexhe et al., 1998) of 5 different amplitudes occurred in a randomized fashion, at 10 Hz, in a synaptic background of fluctuating excitation and inhibition modeled as above. Such a protocol has the advantage of distinguishing two types of inputs: driving AMPA inputs and modulatory background inputs (Shu et al., 2003; Wolfart et al., 2005). To illustrate the new possibilities offered by high resolution recording of spikes using AEC (Figure 6A, "AEC"), we performed an analysis of spike threshold variability. In cortical neurons, the  $V_m$  value at spike threshold has been shown to correlate with the slope of the preceding

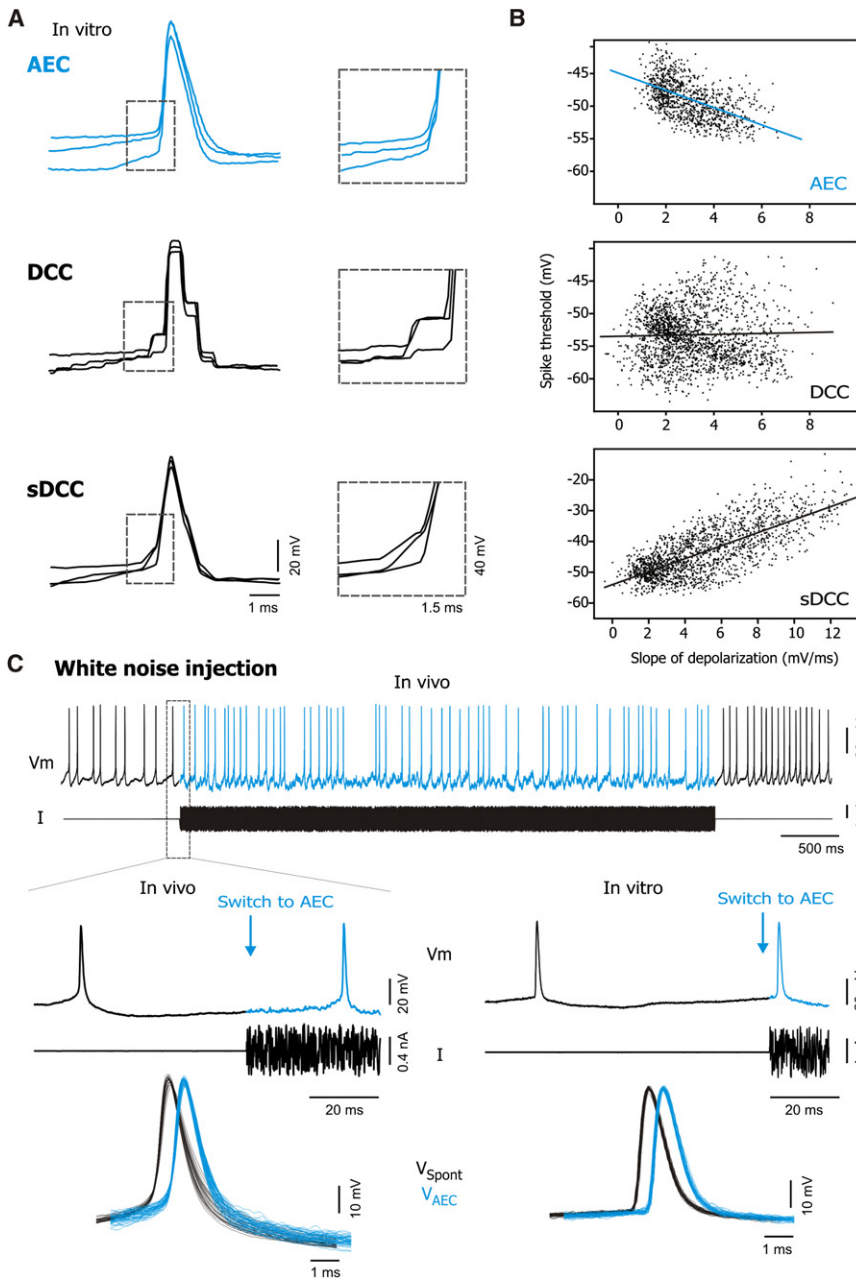


**Figure 6. Spikes Evoked by a Complex Dynamic-Clamp Conductance Injection and Spikes Recorded during White Noise Current Injection**

(A) Examples of single spikes recorded in AEC (blue, top) or DCC (black, middle) for different slopes of depolarization preceding the spike. Spikes obtained when the DCC recording is smoothed are shown at the bottom (“sDCC”). Insets show magnification of the onset of spikes ( $R_e = 64 \text{ M}\Omega$ , RS cell in vitro).

(B) Spike threshold versus slope of depolarization preceding spikes from injections corresponding to the examples shown in (A). Lines are linear regressions to the clouds of points.

(C) Spontaneous spikes (black,  $V_{\text{spont}}$ ) are compared to spikes recorded in the same cell during white noise current injection using AEC (blue,  $V_{\text{AEC}}$ ) in vivo (central trace and magnification; left: RS cell,  $R_e = 104 \text{ M}\Omega$ ) and in vitro (right: IB cell,  $R_e = 91 \text{ M}\Omega$ ).

the threshold, one detects an approximately random value at the beginning of the spike, and so the slope-“threshold” correlation (average slope of linear regression,  $0.5 \text{ ms}$ , range  $0.07$  to  $1.43 \text{ ms}$ ; average coefficient of regression,  $0.177$ , range  $0.028$  to  $0.475$ ) is either nonsignificant ( $2/7$  injections) or positive ( $5/7$  injections): this relation (Figure 6B, “DCC”) reflects the fact that  $V_m$  and  $V_m$  slope are positively correlated along the rising phase of a spike. Smoothing the DCC trace can make the spikes look better by eye (Figure 6A, “sDCC”) but cannot retrieve high frequency information like spike threshold, and so the results of slope-threshold analysis are similar to the ones obtained from a raw DCC trace (significant positive correlation in all 7 cases; average slope of linear regression,  $2.8 \text{ ms}$ , range  $2.1$  to  $4.1 \text{ ms}$ ; average coefficient of regression,  $0.787$ , range  $0.686$  to  $0.895$ ) (Figure 6B, “sDCC”).

depolarization in a way such that faster depolarizations evoke spikes from a more negative threshold (Azouz and Gray, 2000; de Polavieja et al., 2005; Wilent and Contreras, 2005b). We find such a significant negative correlation in all our AEC recordings (average slope of linear regression,  $-1.4 \text{ ms}$ , range  $-3.6$  to  $-0.5 \text{ ms}$ ; average coefficient of regression,  $0.407$ , range  $0.137$ – $0.621$ ), similar to the example shown in the top row of Figure 6B (“AEC”). This analysis cannot be done with DCC recordings because spike threshold is not detected with enough accuracy (Figure 6A, “DCC”): the time of spike onset is not locked to the DCC (low) sampling frequency, and thus, the first  $V_m$  value to be effectively recorded after spike onset is only weakly correlated with the actual  $V_m$  value at spike threshold. Instead of detecting

These recordings were also a good opportunity to test the presence of fast electrode nonlinearities because large negative currents were injected at spike times (up to  $-5 \text{ nA}$ ). We found that the correlation between the injected current and the voltage at spike peaks was very small (between  $-0.1 \text{ M}\Omega$  and  $-0.6 \text{ M}\Omega$ , 4 cells; see Figure S2), confirming the absence of significant fast nonlinearities that would manifest themselves as over- or under-compensation of  $R_e$  during spikes.

In addition, in order to directly convince ourselves that the shape of fast cellular events like spikes is correctly recorded with AEC, we compared 36 spontaneous spikes recorded without any current injection in one cell in vitro to 36 spikes recorded in the same cell using AEC during white noise current injection with  $0 \text{ nA}$

mean (Figure 6C, right bottom). Under these conditions, the average  $V_m$  and the firing frequency were the same so that spike shape was not expected to change due to adaptation. We found no significant difference (unpaired *t* test) between spikes recorded with and without current injection in terms of spike height ( $54.0 \pm 1.5$  mV versus  $53.9 \pm 1.1$  mV, respectively;  $p = 0.8413$ ), spike width at half-amplitude ( $0.91 \pm 0.04$  ms versus  $0.90 \pm 0.03$  ms,  $p = 0.2859$ ), or spike threshold ( $-50.4 \pm 1.3$  mV versus  $-50.9 \pm 1.0$  mV,  $p = 0.0967$ ). Spikes recorded using AEC in vivo were also very similar to spontaneous spikes (Figure 6C, top trace and left bottom). The possibility to precisely analyze spike onset and spike shape during finely controlled current- and dynamic-clamp stimuli, demonstrated here with AEC, but not feasible before with high-resistance electrodes due to the limited sampling frequency of the DCC, appears crucial, especially in the light of recent reports indicating that in cortical networks, spikes are more than all-or-none signals (de Polavieja et al., 2005) and that their shape might influence synaptic transmission and, thus, the functioning of the network (Shu et al., 2006).

## DISCUSSION

In this paper, we have introduced an intracellular recording strategy, Active Electrode Compensation (AEC), which consists of correcting for the electrode bias using a model of the electrode interfaced in real time with the electrophysiological setup. We tested AEC in two classical preparations used in numerous studies of mammalian cortex: visual cortical acute slices and cat primary visual cortex in vivo. We examined different recording situations of increasing levels of complexity, spanning current-clamp and especially dynamic-clamp protocols, which allow the probing of neuronal properties with stimuli closely resembling synaptic inputs received by cortical cells in functioning networks. In each case, we compared AEC recordings with traditional recording techniques, as well as with theoretical predictions when possible. We discuss below the novelty and the domain of applicability of this method.

The AEC method relies on a more powerful model of the electrode than the simple RC model at the basis of most electrode compensation techniques (Purves, 1981; de Sa and MacKay, 2001; Sherman et al., 1999; [http://www.moleculardevices.com/pages/instruments/axon\\_guide.html](http://www.moleculardevices.com/pages/instruments/axon_guide.html); but see Roelfsema et al., 2001) and thus allows accurate intracellular recordings at a high sampling frequency during simultaneous current injection, uncontaminated by capacitive transients. Some new commercial amplifiers propose improved electrode compensation for voltage clamp, but they do not address the same problem as we do here: the VE-2 patch amplifier (Alembic instruments) implements an adjustable model of the electrode, as we do, and an improved algorithm for controlling the cell's voltage after subtraction of the electrode voltage, but the electrode model remains a simple RC one and the method fails when the electrode's behavior is more complex (Sherman et al., 1999); other amplifiers (SEC, from NPI) implement the supercharging technique (Strickholm, 1995; Müller et al., 1999) to speed up the electrode's response by adding brief current pulses to the command current in discontinuous single-electrode voltage-clamp and thus allow a higher switching frequency, but this technique mod-

ifies the total current injected into the cell, and so it is not possible to use it in dynamic clamp to inject a finely controlled current mimicking intrinsic or synaptic ion channels. Besides, all these techniques, which are implemented on manually calibrated analog circuits, are based on simple electrical models of the electrode that cannot fully take the complexity of real electrodes into account. The AEC method uses an arbitrarily complex linear model to compute the electrode's response, does not distort the injected current, does not require manual calibration, and its digital implementation is possible on any computer system adapted to run in real time and interfaced with any standard electrophysiological setup. It is thus not only more efficient, but also more generally applicable, easier to use, and cheaper to implement than any other current electrode compensation technique.

The main condition that has to be met for the method to work accurately is the linearity of the electrode and of the whole recording chain between the electrode and the computer (amplifiers and filters) for the range of expected voltages and currents. The AEC method provides a fast and automated way to measure electrode nonlinearities intracellularly (while with standard techniques, electrode nonlinearities are measured from the I-V curve of the electrode, which could be confused intracellularly with the I-V curve of the neuron), and we found that about half of our electrodes were reasonably linear. In addition, our experiments confirm that electrode nonlinearities are essentially slow, so that large currents that are only transiently injected should not degrade the quality of electrode compensation. As to the rest of the recording chain, its linearity has to be checked in a model electronic cell prior to the use of the method: this condition was satisfied for the Axoclamp 2B/2A and the CyberAmp 380 signal conditioner we tested (data not shown).

Other requirements are similar to the requirements of classical methods, such as "bridge" compensation or DCC. For optimal separation between cell and electrode kernels, their time constants have to be maximally different, which means that the capacitance neutralization provided by the amplifier should be used optimally like in the other methods. However, numerical simulations show that AEC can work with electrodes only ten times faster than the membrane, while DCC requires electrodes about 100 times faster than the membrane (Figures S1D and S3; see also Brette et al., 2007); thus, AEC should extend the applicability of single-electrode recordings to neurons with much shorter time constants. As with the other methods, if electrode properties change during the recording, the compensation has to be readjusted; however, a 5 s white noise injection was sufficient in our hands to get a reliable electrode kernel estimation in vitro, and so this re-estimation is not more time consuming than with "bridge" compensation or DCC. This minimal length of white noise injection can increase if the cell's response is noisier (in vivo, we used mainly 20 s), so this parameter should be optimized for each preparation. However, once the right parameters such as kernel size and white noise injection length are chosen for a given preparation, the procedure is fully automatic.

Three limitations have to be mentioned, even if they are present in all other recording modes, including two-electrode recordings. First, the injected current is still filtered by the electrode. However, in the case of the AEC method, the true injected current can be approximately estimated offline from the knowledge of the electrode

kernel. Second, strong current generated by the cell (i.e., during spikes) affects the electrode response but is not taken into account by the compensation method, and so spikes are still filtered by the electrode (Figure S3). This last effect can be reduced by the capacitance neutralization of the amplifier, which is a second reason for using this control together with AEC. Third, the problem of space clamp, which limits the control of the dendritic tree during somatic recordings, is still present (however, AEC could improve the feasibility of dendritic recordings, see below).

The tests we performed *in vitro* and *in vivo* indicate that while for low frequency information, the DCC method presents no severe disadvantage over the high-resolution AEC method, applications requiring high-frequency sampling in single high-resistance electrode recordings are only possible with AEC. We showed that recording responses to white noise current injection at 10 kHz is now feasible and that dynamic clamp gains an unprecedented accuracy, allowing to analyze precise features of the spiking response during a finely controlled *in vivo*-like conductance-based stimulus. It thus becomes possible to stimulate neurons with fast and dynamically varying stimuli and to simultaneously record their response at the time-scale of the stimulus without loss of accuracy. It should be stressed that the current temporal resolution of the method (10 kHz) is only limited by computer processor speed: it could be increased through implementation on a devoted chip, and its advantage over classical discontinuous methods can be expected to grow substantially in the coming years.

The possibility offered by AEC to perform accurate recordings during fast current and conductance injections *in vivo*, using sharp electrodes, greatly improves the feasibility of such protocols *in vivo* by overcoming the need to obtain very low access resistance. Moreover, our simulations (Figure S3) show that AEC could be used when electrode and membrane time constants are not very different, while DCC cannot be applied in this case. This situation is observed especially during *in vivo* patch recordings, where the time constant of the electrode is large (e.g., Anderson et al., 2000) so that in this case, the AEC technique should be a great advantage as well. Dendritic and axonic patch clamp *in vitro*, requiring much finer and thus higher series resistance electrodes than classical whole-cell recordings (>20 M $\Omega$ , Davie et al., 2006), could be another potential field of application. We are also currently exploring the applicability of AEC to single-electrode voltage-clamp protocols. We thus expect AEC to allow many interesting studies like the *in vivo* exploration of the role of various intrinsic channels specific to different cortical cell types, the *in vivo* mimicking of the effects of neuromodulators on specific channels at the single-cell level, or the precise manipulation of conductance-based synaptic inputs onto dendrites.

## EXPERIMENTAL PROCEDURES

The Supplemental Data provide additional details.

### Biological Preparation, *In Vitro*

We prepared 380  $\mu$ m thick coronal or sagittal slices from the lateral portions of 4- to 12-week-old guinea pig (CPA, Olivet, France) occipital cortex, as well as from adult ferret (Marshall, France) occipital cortex in some early experiments, as described previously (Rudolph et al., 2004; Pospischil et al., 2007). Slices were maintained in an interface style recording chamber at 33°C–35°C in slice solution containing (in mM) 124 NaCl, 2.5 KCl, 1.2 MgSO<sub>4</sub>, 1.25 NaHPO<sub>4</sub>,

2 CaCl<sub>2</sub>, 26 NaHCO<sub>3</sub>, and 10 or 25 dextrose and aerated with 95% O<sub>2</sub> and 5% CO<sub>2</sub> to a final pH of 7.4. Intracellular recordings were performed in all cortical layers after 2 hr of recovery. All procedures adhered to American and European ethical guidelines (see the Supplemental Data).

### Biological Preparation, *In Vivo*

All surgical procedures were performed in conformity with national (JO 87-848) and European legislation (86/609/CEE) on animal experimentation and strictly following the recommendations of the Physiological Society, the European Commission, and the NIH. Cats were initially anesthetized with althesin (Glaxo; 1:2 ml/kg; 10:8 mg/kg alfaxalone and 3:6 mg/kg alfadolone acetate given by intramuscular injection). Following tracheotomy, animals were artificially ventilated and anesthetized with an intravenous flow of althesin (3 mg/kg/hr) and pancromium bromide (0:2 mg/kg/hr) supplemented with glucose and isotonic saline. ECG and EEG were continuously monitored during the experiment and body temperature was maintained at 37°C. The artificial respiration rate was set to 25 beats/min. and the volume of inhaled air adjusted to maintain expired pCO<sub>2</sub> between 3.8% and 4.2%. Intracellular recordings were performed in the area centralis representation (Horsley-Clarke coordinates P: 1:5-2:5, L: 1:5) in cat area 17.

### Electrophysiology

Sharp electrodes for intracellular recordings were made on a Sutter Instruments P-87 or P-97 micropipette puller from medium-walled glass (WPI, 1BF100 *in vitro*; WPI, 1B150F-4 *in vivo*) and beveled (*in vitro*) on a Sutter Instruments beveller (BV-10M), or not (*in vivo*). Micropipettes were filled with 1.2–2 M potassium acetate (*in vitro*) or 2 M potassium methyl sulfate (*in vivo*) with 4 mM potassium chloride and had resistances of 65–110 M $\Omega$ . Axoclamp 2B (*in vitro*) or 2A (*in vivo*) amplifiers (Axon Instruments) were used either in continuous current-clamp (“bridge”) mode or in discontinuous current-clamp (DCC) mode. In both cases, the capacitance neutralization was set at the maximal possible value to achieve the fastest possible electrode charging time (see the Supplemental Data). For both *in vitro* and *in vivo* experiments, a Digidata 1322A card (Axon Instruments) and the PC-based software ELPHY (developed by G. Sadoc, UNIC, CNRS) were used for data acquisition at 20 kHz.

### Real-Time Computer Implementation

We used the hybrid RT-NEURON environment (developed by G. Le Masson, INSERM 358, Université Bordeaux 2; Gérard Sadoc, CNRS), a modified version of NEURON (Hines and Carnevale, 1997) running under the Windows 2000 operating system (Microsoft) on a single core 2GHz Pentium desktop PC. To achieve real-time electrode compensation and simulation of synaptic inputs (dynamic clamp) as well as data transfer to the PC for further analysis, we used a PCI DSP board (Innovative Integration) with four analog/digital (inputs) and four digital/analog (outputs) 16-bit converters. The DSP board constrains calculations made by NEURON and data transfers to be made with a high priority level by the PC processor. The DSP board allows input (the total recorded potential  $V_m + U_e$  to be compensated, and then incorporated in the equations of the models in the dynamic-clamp case) and output signals (the current to be injected into the cell; the compensated  $V_m$  for the acquisition system) to be processed at regular intervals (0.1 ms time resolution). A custom interface or a CyberAmp 380 (Axon Instruments) were used to low-pass filter, at 6 kHz, the analog input/output signals of the DSP board and to adjust their ranges in order to improve the digitalization resolution. The full RT-NEURON code used in our experiments, as well as some sample code implementing the AEC on different platforms, can be found at <http://www.di.ens.fr/~brette/HRCORTEX/AEC/AECcode.html>.

### Data Analysis

The PC-based software ELPHY, Matlab (The Mathworks, Natick, MA), Scilab (INRIA/ENPC, <http://www.scilab.org>), and custom-written C-code were used. All statistical tests were performed using the software Statview 5.0 (SAS Institute, Cary, NC). All values are given as average  $\pm$  standard deviation or, for small sample size, as average and range. A p value < 0.05 was required for statistical significance. Passive neuron parameters (input resistance and membrane capacitance) were derived from responses to small current pulses, and  $E_{\text{peak}} = V_{\text{rest}}$ . Detailed data analysis procedures are given in Supplemental Data.

### Estimation of the Electrode Kernel

In order to probe the electrode, we inject a known time-varying current  $I(n)$  ( $n$  is the number of the sampling step) and measure the response  $V_r(n)$  for a duration of  $N$  sampling steps (we used 5–20 s, i.e., 50,000–200,000 steps). The kernel  $K$  is calculated so that the convolution  $K * I(n)$  is the best estimation of  $V_r(n)$  in the least square sense. In practice, the kernel  $K$  is finite and consists of  $M$  sampling steps (we used  $M = 150$ – $200$ , corresponding to 15–20 ms). For algorithmic reasons (see [Supplemental Data](#)), the injected current  $I(n)$  must vanish in the last  $M$  sampling steps of the recording. Then, the optimal kernel values correspond to the solutions of a matrix problem  $AX = B$ , where the coefficients of matrix  $A$  and vector  $B$  are the autocorrelation coefficients of the current ( $\sum_{n=0}^{N-p} I(n)I(n-p)$ ) and the current-voltage correlation coefficients ( $\sum_{n=0}^{N-p} V_r(n)I(n-p)$ ). These coefficients can be calculated recursively online without storing the values  $V_r(n)$  and  $I(n)$ . The matrix  $A$  has a special structure (symmetrical Toeplitz matrix), so that the matrix equation can be solved very efficiently with the Levinson algorithm (Press et al., 1993).

The kernel we obtain combines the electrode kernel  $K_e$  and the membrane kernel  $K_m$ . For small currents, the membrane potential can be expressed as the convolution  $V_m = V_{rest} + K_m * I_m$ , where  $I_m$  is the current entering the membrane. The injected current  $I_e$  is filtered through the electrode before entering the membrane. We approximate this filtering by the convolution  $I_m = (K_e/R_e) * I_e$ , where  $R_e = \int K_e$  is the electrode resistance. Thus, the total filter  $K$  that we measured can be expressed as:

$$K = K_e + K_m * \frac{K_e}{R_e} \quad (2)$$

In order to retrieve the electrode kernel  $K_e$ , we need to determine the membrane kernel  $K_m$  and invert the relationship above. We approximate  $K_m$  by an exponential function:  $K_m(t) = \frac{R}{\tau} e^{-t/\tau}$ , and we estimate the time constant  $\tau$  by fitting an exponential function to the tail of the kernel  $K$  (typically  $t > 5$  ms), which is correct if the electrode is faster than the membrane. From this fit, we obtain an estimation  $R'$  of the membrane resistance. It is an overestimation because the electrode delays the response of the membrane. The electrode resistance  $R_e$  is then estimated as  $R_e' = \int K - R'$ . In practice, we have only a truncated version of the full kernel (typically the first 15–20 ms), so that only part of the membrane resistance must be subtracted. Once estimates have been derived for  $R$ ,  $R_e$ , and  $\tau$ , it is possible to deduce  $K_e$  from  $K$ . We solve Equation 2 by applying the Z-transform, which transforms convolutions into multiplications (see [Supplemental Data](#)).

Finally, we refine the electrode kernel as follows: if the estimates of  $R$  and  $R_e$  were correct, then the tail of the kernel ( $t > 5$  ms) should vanish. If there is a positive remainder, then  $R$  was underestimated; if there is a negative remainder, then it was overestimated. Therefore, in order to reach the best precision, we reiterate the procedure with different estimates for  $R$  (and corresponding estimates for  $R_e$ ) using the golden section search algorithm (Press et al., 1993), so as to minimize the tail of the estimated kernel  $K_e$ .

### SUPPLEMENTAL DATA

The Supplemental Data include Supplemental Experimental Procedures, Supplemental References, and six figures and can be found with this article online at <http://www.neuron.org/cgi/content/full/59/3/379/DC1>.

### ACKNOWLEDGMENTS

We thank Paul Galloux, Gérard Sadoc, Jose Gomez, and Leonel Gomez for help with the real-time system and for stimulating discussions. This work was supported by CNRS, ANR (HR-CORTEX grant), ACI, HFSP, and the European Community (FACETS grant FP6 15879). Z.P. gratefully acknowledges the support of the FRM.

Accepted: June 16, 2008  
Published: August 13, 2008

### REFERENCES

- Anderson, J.S., Carandini, M., and Ferster, D. (2000). Orientation tuning of input conductance, excitation, and inhibition in cat primary visual cortex. *J. Neurophysiol.* 84, 909–926.
- Azouz, R., and Gray, C.M. (2000). Dynamic spike threshold reveals a mechanism for synaptic coincidence detection in cortical neurons in vivo. *Proc. Natl. Acad. Sci. USA* 97, 8110–8115.
- Borg-Graham, L.J., Monier, C., and Frégnac, Y. (1998). Visual input evokes transient and strong shunting inhibition in visual cortical neurons. *Nature* 393, 369–373.
- Brennecke, R., and Lindemann, B. (1971). A chopped-current clamp for current injection and recording of membrane polarization with single electrodes of changing resistance. *TIT J. Life Sci.* 1, 53–58.
- Brennecke, R., and Lindemann, B. (1974a). Theory of a membrane-voltage clamp with discontinuous feedback through a pulsed current clamp. *Rev. Sci. Instrum.* 45, 184–188.
- Brennecke, R., and Lindemann, B. (1974b). Design of a fast voltage clamp for biological membranes, using discontinuous feedback. *Rev. Sci. Instrum.* 45, 656–661.
- Brette, R., Piwkowska, Z., Rudolph, M., Bal, T., and Destexhe, A. (2007). A non-parametric electrode model for intracellular recording. In *Proceedings of CNS 2006* (Edinburgh, UK). Neurocomputing 70, 1597–1601.
- Bryant, H.L., and Segundo, J.P. (1976). Spike initiation by transmembrane current: a white-noise analysis. *J. Physiol.* 260, 279–314.
- Crochet, S., Fuentealba, P., Cisse, Y., Timofeev, I., and Steriade, M. (2006). Synaptic plasticity in local cortical network in vivo and its modulation by the level of neuronal activity. *Cereb. Cortex* 16, 618–631.
- Davie, J.T., Kole, M.H., Letzkus, J.J., Rancz, E.A., Spruston, N., Stuart, G.J., and Hausser, M. (2006). Dendritic patch-clamp recording. *Nat. Protocols* 1, 1235–1247.
- de Polavieja, G.G., Harsch, A., Kleppe, I., Robinson, H.P., and Juusola, M. (2005). Stimulus history reliably shapes action potential waveforms of cortical neurons. *J. Neurosci.* 25, 5657–5665.
- de Sa, V.R., and MacKay, D.J.C. (2001). Model fitting as an aid to bridge balancing in neuronal recording. *Neurocomputing* 38–40, 1651–1656.
- Destexhe, A., Mainen, Z.F., and Sejnowski, T.J. (1998). Kinetic models of synaptic transmission. In *Methods in Neuronal Modeling*, C. Koch and I. Segev, eds. (Cambridge, Massachusetts: MIT press), pp. 1–26.
- Destexhe, A., and Rudolph, M. (2004). Extracting information from the power spectrum of synaptic noise. *J. Comput. Neurosci.* 17, 327–345.
- Destexhe, A., Rudolph, M., Fellous, J.M., and Sejnowski, T.J. (2001). Fluctuating synaptic conductances recreate in vivo-like activity in neocortical neurons. *Neuroscience* 107, 13–24.
- Destexhe, A., Rudolph, M., and Paré, D. (2003). The high-conductance state of neocortical neurons in vivo. *Nat. Rev. Neurosci.* 4, 739–751.
- Finkel, A.S., and Redman, S. (1984). Theory and operation of a single micro-electrode voltage clamp. *J. Neurosci. Methods* 11, 101–127.
- Haider, B., Duque, A., Hasenstaub, A.R., Yu, Y., and McCormick, D.A. (2007). Enhancement of Visual Responsiveness by Spontaneous Local Network Activity in vivo. *J. Neurophysiol.* 97, 4186–4202.
- Higley, M.J., and Contreras, D. (2007). Cellular mechanisms of suppressive interactions between somatosensory responses in vivo. *J. Neurophysiol.* 97, 647–658.
- Hines, M.L., and Carnevale, N.T. (1997). The NEURON simulation environment. *Neural Comput.* 9, 1179–1209.
- Hirsch, J.A., Alonso, J.M., Reid, R.C., and Martinez, L.M. (1998). Synaptic integration in striate cortical simple cells. *J. Neurosci.* 18, 9517–9528.
- Margrie, T.W., Brecht, M., and Sakmann, B. (2002). In vivo, low-resistance, whole-cell recordings from neurons in the anaesthetized and awake mammalian brain. *Pflügers Arch.* 444, 491–498.

- Mokeychev, A., Okun, M., Barak, O., Katz, Y., Ben-Shahar, O., and Lampl, I. (2007). Stochastic emergence of repeating cortical motifs in spontaneous membrane potential fluctuations in vivo. *Neuron* 53, 413–425.
- Monier, C., Fournier, J., and Frégnac, Y. (2008). *In vitro* and *in vivo* measures of evoked excitatory and inhibitory conductance dynamics in sensory cortices. *J. Neurosci. Methods*. 10.1016/j.jneumeth.2007.11.008.
- Müller, A., Lauven, M., Berkels, R., Dhein, S., Polder, H.-R., and Klaus, W. (1999). Switched single-electrode voltage-clamp amplifiers allow precise measurement of gap junction conductance. *Am. J. Physiol. Cell Physiol.* 276, 980–987.
- Paz, J.T., Chavez, M., SAILLET, S., Deniau, J.M., and Charpier, S. (2007). Activity of ventral medial thalamic neurons during absence seizures and modulation of cortical paroxysms by the nigrothalamic pathway. *J. Neurosci.* 27, 929–941.
- Pei, X., Volgushev, M., Vidyasagar, T.R., and Creutzfeldt, O.D. (1991). Whole-cell recording and conductance measurements in cat visual cortex in vivo. *Neuroreport* 2, 485–488.
- Pospischil, M., Piwkowska, Z., Rudolph, M., Bal, T., and Destexhe, A. (2007). Calculating event-triggered average synaptic conductances from the membrane potential. *J. Neurophysiol.* 97, 2544–2552.
- Press, W.H., Flannery, B.P., Teukolsky, S.A., and Vetterling, W.T. (1993). *Numerical Recipes in C: The Art of Scientific Computing* (Cambridge, New York: Cambridge University Press).
- Prinz, A.A., Abbott, L.F., and Marder, E. (2004). The dynamic clamp comes of age. *Trends Neurosci.* 27, 218–224.
- Purves, R.D. (1981). *Microelectrode methods for intracellular recording and iontophoresis* (London, New York: Academic Press).
- Robinson, H.P., and Kawai, N. (1993). Injection of digitally synthesized synaptic conductance transients to measure the integrative properties of neurons. *J. Neurosci. Methods* 49, 157–165.
- Roelfsema, M.R., Steinmeyer, R., and Hedrich, R. (2001). Discontinuous single electrode voltage-clamp measurements: assessment of clamp accuracy in *Vicia faba* guard cells. *J. Exp. Bot.* 52, 1933–1939.
- Rudolph, M., and Destexhe, A. (2003). Characterization of subthreshold voltage fluctuations in neuronal membranes. *Neural Comput.* 15, 2577–2618.
- Rudolph, M., Piwkowska, Z., Badoual, M., Bal, T., and Destexhe, A. (2004). A method to estimate synaptic conductances from membrane potential fluctuations. *J. Neurophysiol.* 91, 2884–2896.
- Sharp, A.A., O'Neil, M.B., Abbott, L.F., and Marder, E. (1993). The dynamic clamp: artificial conductances in biological neurons. *Trends Neurosci.* 16, 389–394.
- Sherman, A.J., Shrier, A., and Cooper, E. (1999). Series resistance compensation for whole-cell patch-clamp studies using a membrane state estimator. *Biophys. J.* 77, 2590–2601.
- Shu, Y., Hasenstaub, A., Badoual, M., Bal, T., and McCormick, D.A. (2003). Barrages of synaptic activity control the gain and sensitivity of cortical neurons. *J. Neurosci.* 23, 10388–10401.
- Shu, Y., Hasenstaub, A., Duque, A., Yu, Y., and McCormick, D.A. (2006). Modulation of intracortical synaptic potentials by presynaptic somatic membrane potential. *Nature* 441, 761–765.
- Steriade, M., Timofeev, I., and Grenier, F. (2001). Natural waking and sleep states: a view from inside neocortical neurons. *J. Neurophysiol.* 85, 1969–1985.
- Strickholm, A. (1995). A supercharger for single electrode voltage and current clamping. *J. Neurosci. Methods* 61, 47–52.
- Thomas, M.V. (1977). Microelectrode amplifier with improved method of input-capacitance neutralization. *Med. Biol. Eng. Comput.* 15, 450–454.
- Thomson, A.M., and Deuchars, J. (1997). Synaptic interactions in neocortical local circuits: dual intracellular recordings in vitro. *Cereb. Cortex* 7, 510–522.
- Wehr, M., and Zador, A.M. (2003). Balanced inhibition underlies tuning and sharpens spike timing in auditory cortex. *Nature* 426, 442–446.
- Wilent, W.B., and Contreras, D. (2005a). Dynamics of excitation and inhibition underlying stimulus selectivity in rat somatosensory cortex. *Nat. Neurosci.* 8, 1364–1370.
- Wilent, W.B., and Contreras, D. (2005b). Stimulus-dependent changes in spike threshold enhance feature selectivity in rat barrel cortex neurons. *J. Neurosci.* 25, 2983–2991.
- Wolfart, J., Debay, D., Le Masson, G., Destexhe, A., and Bal, T. (2005). Synaptic background activity controls spike transfer from thalamus to cortex. *Nat. Neurosci.* 8, 1760–1767.